Synthesis and Optical Properties of One-Year Air-Stable Chiral Sb(III) Halide Semiconductors

Ali Azmy,[1] Daria M. Konovalova,[1] Leah Lepore,[1] Alexander Fyffe,[2] Doyun Kim,[3] Lukasz Wojtas,[1] Qing Tu,[3] Minh Tuan Trinh,[4] Nourdine Zibouche*,[5] and Ioannis Spanopoulos*,[1]

[1]Department of Chemistry, University of South Florida, Tampa, Florida 33620, United States
[2]Department of Physics, University of South Florida, Tampa, Florida 33620, United States
[3] Department of Materials Science & Engineering, Texas A&M University, College Station, Texas 77840, United States
[4]Department of Chemistry and Biochemistry, Utah State University, Logan 84322, United States
[5]Department of Chemistry, University of Lancaster, Lancaster, LA1 4YW, United Kingdom

ABSTRACT

Chiral hybrid metal-halide semiconductors (MHS) pose as ideal candidates for spintronic applications owing to their strong spin-orbit coupling (SOC), and long spin relaxation times. Shedding light on the underlying structure-property relationships is of paramount importance for the targeted synthesis of materials with optimum performance. Herein, we report the synthesis and optical properties of 1D chiral (R-/S-THBTD)SbBr$_5$ (THBTD = 4,5,6,7-tetrahydro-benzothiazole-2,6-diamine) semiconductors using a multifunctional ligand as a counter-cation and a structure directing agent. (R-/S-THBTD)SbBr$_5$ feature direct and indirect bandgap characteristics, exhibiting photoluminescence (PL) light emission at RT that is accompanied by a lifetime of 4 ns. Circular dichroism (CD), second harmonic generation (SHG), and piezoresponse force microscopy (PFM) studies validate the chiral nature of the synthesized materials. Density functional theory (DFT) calculations revealed a Rashba/Dresselhaus (R/D) spin-splitting, supported by an energy splitting (E_R) of 23 meV and 25 meV, and a Rashba parameter (α_R) of 0.23 eV·Å and 0.32 eV·Å for the R and S analogs respectively. These values are comparable to those of 3D and 2D perovskite materials. Notably, (S-THBTD)SbBr$_5$ is air-stable for a year, a record performance for chiral lead-free MHS. This work demonstrates that low-dimensional, lead-free, chiral semiconductors with exceptional air stability can be acquired, without compromising spin splitting and manipulation performance.

INTRODUCTION

Hybrid (organic-inorganic) metal-halide semiconductors (MHS) is a versatile class of materials,[1,2] exploited for a plethora of applications spanning from photovoltaics[3-4] and photocatalysis,[5-6] to light detection[7-8] and emission.[9-10] Their hybrid nature allows for manipulation of their structural,[11-12] mechanical[13-14] and optoelectronic[15-17] properties to an extent that is difficult to be realized by other classes of semiconductors. Of particular interest are the chiral MHS, which have proven to be quite promising for cutting-edge applications such as circularly polarized light (CPL) emission and detection,[18-19] non-linear optics (NLO),[20-21] piezoelectric energy harvesting,[22-23] and spintronics.[24-25] In the latter case, specific MHS attributes, such as the presence of large and tunable spin–orbit coupling (SOC),[26] spin-dependent optical selection rules[27-28] and tunable Rashba/Dresselhaus (R/D) spin splitting,[29-30] render them exceptional candidates for next generation spin-orbitronic and quantum computing devices.[31-33] In terms of materials engineering, all the above parameters can be modeled and incorporated into a single crystalline structure.[34] The presence of heavy elements, such as Pb, Bi, and Sb can give rise to strong SOC, while the acquisition of a non-centrosymmetric structure, by using a chiral organic linker as structure directing agent and counter cation, can provide crystalline compounds that exhibit a large R/D effect.[35] Notably, spin manipulation by means of spin-splitting can be further achieved by kinetically controlled structural transitions, as it was reported recently by Xie et al.,[36] or by means of chiral induction based on the work of Zheng et al.[37]

Since the first report of enantiopure chiral MHS in 2003,[38] multiple studies have enriched the field. However, the majority is based on Pb(II) compounds using a limited number of chiral organic linkers, such as α-phenylethylamine (α-PEA),[39] ((R)-β-MPA = (R)-(+)-β-methylphenethylamine,[40] (R-/S-MBA) MBA = methylbenzylammonium,[27, 41-43] (R-S-NEA) NEA = -(2-naphthyl)ethylamine[44-45] and (R-BPEA) (R-BPEA = (R)-1-(4-bromophenyl)ethylammonium).[46] Considering the toxicity of Pb(II), research interest moved towards the utilization of non-toxic, heavy cations such as Bi(III)[47-52] and Sb(III) [37, 53-58] for the synthesis of chiral MHS.

The development of new lead-free chiral MHS constitutes a platform for shedding light on underlying structure-property relationships in terms of R/D spin splitting for efficient spin manipulation. In return, this could be of paramount

importance for the design of next generation semiconductors for spintronic applications. Another feature that must be considered is the long-term environmental stability of the corresponding materials, a crucial information that seems to be neglected. This trait ensures not only proper materials characterization, but also paves the way for commercialization.[59] Although there are some studies evaluating the stability of various lead-free metal halides based on Bi(III) and Sb(III) for up to a year,[60-63] there are only scarce reports about the environmental stability of chiral lead-free MHS. In particular, Wu et al. developed a 1D semiconductor, namely $(C_9H_{14}N)SbCl_4$ ($C_9H_{14}N$ = N,N,4-trimethylaniline) with high second harmonic generation (SHG) response, which is air-stable for 3 months,[58] Moon et al. reported the synthesis of 0D $[((R/S)-C_8H_{12}N)_4][Bi_2Br_{10}]$, ($C_8H_{12}N$ = 1-phenyl-ethylammonium) which is stable in humid air for 1 month,[50] Tao et al., acquired the 0D (R-α-PEA)$_4$Bi$_2$I$_{10}$ and (S-α-PEA)$_4$Bi$_2$I$_{10}$ compounds which are air stable for 4 months,[64] while Maiti et al., synthesized the 0D (R/S-MBA)$_4$Bi$_2$Br$_{10}$ materials which are air stable for 15 days.[65]

Towards addressing the above concerns, we report here the synthesis of chiral (R-/S-THBTD)SbBr$_5$ (THBTD = 4,5,6,7-tetrahydro-benzothiazole-2,6-diamine) semiconductors, using an unexplored multifunctional chiral linker as a structure directing agent. Both R and S enantiomers crystallize in the polar space group $P2_1$, giving rise to a 1D corrugated structure consisting of corner sharing [SbBr$_6$]$^{3-}$ octahedra. (R-/S-THBTD)SbBr$_5$ feature direct and indirect bandgap characteristics, exhibiting broad band edge light emission at RT that is accompanied by a lifetime of 4 ns. Circular dichroism (CD), second harmonic generation (SHG) and piezoresponse force microscopy (PFM) studies validate the chiral nature of the corresponding materials, while density functional theory (DFT) calculations revealed the R/D energy spin splitting, which is comparable to other low dimensional perovskite and metal halide compounds.[66] Notably, the materials are air stable for a year, a record stability among chiral lead-free metal halide semiconductors. All the above traits render (R-/S-THBTD)SbBr$_5$ excellent candidates for elucidating the structure-property relationships that govern the magnitude of the R/D effect.

RESULTS AND DISCUSSION

Synthetic aspects and structural characterization

Pale yellow single crystals of (*R*-/*S*-THBTD)SbBr$_5$ (*R* or *S*) can be acquired through the reaction of Sb(III) oxide and the chiral ligand in a hot HBr solution. Scanning electron microscopy (SEM) measurements revealed well-faceted rectangular block crystals (Figure S1), while energy-dispersive X-ray spectroscopy (EDS) studies confirmed the (*R*-THBTD)SbBr$_5$ formula, giving an Sb: Br ratio of 1:4.9 (Figure S2). Single crystal X-ray diffraction (XRD) studies demonstrated that both enantiomers are isostructural, crystallizing in the monoclinic polar space group *P*2$_1$ (Figures 1, 2 and Table 1). The structure consists of 1D corrugated antiparallel chains of distorted, corner-sharing [SbBr$_6$]$^{3-}$ octahedra that are separated and charge balanced by the chiral molecules. Adjacent inorganic chains are eclipsed along the *α* axis lying at a distance of ~4 Å. Each chain is based on two types of [SbBr$_6$]$^{3-}$ octahedra, deriving from two crystallographically independent Sb atoms and ten Br atoms.

Examining closer the *R* analog, corresponding Sb(1)-Br and Sb(2)-Br bond lengths span from 2.5264(18) Å to 3.2966(19) Å, and 2.5253(18) Å to 3.251(2) Å respectively (Table S3). Similar variation is observed for the Br-Sb-Br angles that range from 83.58(5)° to 177.03(6)° for the cis and trans arrangements respectively (Table S4). Although the Sb lone pair is not stereochemically active, there is still a small degree of octahedral distortion which is ascribed to the presence of multiple moderate hydrogen bonds, ranging from 2.5 Å to 2.8 Å, among the hydrogen atoms of the amine groups of the organic counter-cations and the axial and equatorial bromide atoms of the octahedra (Figure 3). This magnitude of the hydrogen bonds is responsible for asymmetric helical 2$_1$ screw distortions in the octahedra, causing the asymmetrization of the inorganic chain, thus breaking the centrosymmetricity of the structure.

The octahedral distortion can further be quantitatively evaluated by the calculated bond length distortion (Δd), $\Delta d = \frac{1}{6}\sum_{i=1}^{6}\left(\frac{di^{2\square}-d_0{}^2}{d_0{}^2}\right)$, ($d_i$ are the six Sb−Br bond lengths and d_0 is the mean Sb−Br bond length within an octahedron), and bond angle variance (σ^2), $\sigma^2 = \frac{1}{11}\sum_{i=1}^{12}\left(\theta_i - 90\,°\right)^2$, ($\theta_i$ are the 12 Br−Sb−Br bond angles within an octahedron).[67-69] The corresponding values for $[Sb(1)Br_6]^{3-}$ and $[Sb(2)Br_6]^{3-}$ of 0.09 and 22.25 deg.^{2} and 0.09 and 15.08 deg.^{2} for Δd and σ^2 respectively, correlate well with other distorted 1D bromoantimonates(III) based on corner sharing $[SbBr_6]^{3-}$ octahedra, such as $(R\text{-EBAH})_2SbBr_5$ (EBAH = (R)-(+)-α-ethylbenzylammonium) and [3-hydroxy-azetidinium]$_2$SbBr$_5$.[55, 70] It is pointed out that there are very few literature reports of the same 1D structural motif, despite the fact that it can be templated by using both mono and double protonated organic counter cations, as in the cases of $(AMPY)BiI_5$, $(C_3H_7NH_3)_3SnI_5$ and $(piperidinium)_2SbCl$.[71-73]

The organic counter-cations are eclipsed along the a axis, featuring an anti-configuration of brick wall packing arrangement at a distance of 3.3 Å. Under current reaction conditions only two of the three amine groups are protonated, the aliphatic primary amine ($R\text{-NH}_3$) and the aromatic secondary amine (-NH=), which are the most basic ones. The lone pair of the nitrogen atom of the aromatic primary amine is in conjunction with the aromatic thiazole ring, rendering the group significantly less basic than the other two. Interestingly, this asymmetric protonation of the functional groups templated the corresponding uncommon structural motif.

In-house powder X-ray diffraction studies (PXRD) verified the uniform phase purity and record air stability of the corresponding materials, as the experimental and calculated patterns from single crystal XRD studies are identical (Figure 4a). We point out that during the crystallization of the $(R\text{-THBTD})SbBr_5$ enantiomer, another crystal phase was identified based on PXRD studies (Figure S3a). Single crystal XRD studies revealed a structure with the same general formula as the $(R\text{-THBTD})SbBr_5$ main phase, crystallizing in the $P2_1$ space group. The notation $(R\text{-imp})SbBr_5$ will be used to describe the impurity phase throughout this work. $(R\text{-imp})SbBr_5$ is composed of the same type of corrugated inorganic chains as the pure enantiomers, albeit much less distorted, as evident by the corresponding Δd and σ^2 values of 0.06 and 16.71 deg.^{2} respectively. The different packing arrangement of the organic part, where

THBTD cations are displaced in-plane along their stacking axis to a lower extent, as compared to the higher offset arrangement in the pure enantiomers, is responsible for the lower degree of distortion (Figures 5 and 1 respectively). In this regard, corresponding moderate hydrogen bonds among the equatorial and axial Br atoms and the aliphatic $R-NH_3^+$ hydrogens are located on opposite sides of the octahedra (top and bottom), whereas in pure enantiomers these interactions are located on one side only (bottom), thus leading to an asymmetric distortion of the octahedra (Figure S4). In our quest to acquire phase pure R and S materials, we realized that the commercially available ligands were purchased from different suppliers and were of different purity, 95% for the R versus 97% for the S. Upon replacing the 95% R analog with a 97% one, a phase pure $(R\text{-THBTD})SbBr_5$ was acquired, as demonstrated by PXRD studies (Figure S3b).

Thermogravimetric (TGA) analysis demonstrated that the chiral materials are thermally stable up to 220 °C, where a sharp weight loss appears. There are two decomposition steps at ~220 °C and ~350 °C (Figure S5a). The first weight loss (~80%) corresponds to the decomposition of the organic part of the structure and HBr along with $SbBr_3$; the second step (~10%) can be potentially ascribed to the further sublimation of $SbBr_3$, in agreement with previous studies on bromoantimonates(III).[56,74] Differential scanning calorimetry (DSC) measurements support the absence of phase transitions in the examined temperature range (25 – 250 °C) (Figure S5b).

DFT studies

The electronic structure and optical properties of these chiral MHS materials have been investigated using density functional theory (DFT) calculations with SOC included (see Supporting Information for computational details). The band structures of $(R\text{-THBTD})SbBr_5$ and $(S\text{-THBTD})SbBr_5$ are shown in Figure 6 (a and b, respectively). Both materials exhibit a direct and indirect band gap character due to the R/D effect; at the high-symmetry X point for the former and near the high-symmetry Z point of the Brillouin zone (BZ) for the latter, with values for the indirect/direct transitions of 2.28/2.303 eV and 2.30/2.325 eV, respectively. These values are a little lower than the experimental ones, (for the indirect transition: 2.65 eV and 2.62 eV for the S and R analogs, for the direct transition 2.82 eV and 2.80 eV for the S and R analogs respectively, see next section), due to the chosen level of theory (Here DFT-PBE). Similar to the intrinsic inversion symmetry breaking in two-

dimensional (2D) metal halide perovskites, these MHSs also exhibit strong SOC effects in their valence and conduction bands, as shown by the splitting bands near the band edges in the insets of Figure 6. Our calculations reveal the presence of significant Rashba parameters and energies in both compounds. Specifically, the calculated values of the Rashba parameters (α_R) and energies (E_R) in the conduction region are found to be as large as 0.23 eV·Å and 23 meV for (R-THBTD)SbBr$_5$ around the high-symmetry point X and 0.32 eV·Å and 25 meV for (S-THBTD)SbBr$_5$ along the high-symmetry line Z-H, respectively. These values correlate pretty well to higher dimensionality MHS, such as 2D (phenylethylammonium)$_2$PbI$_4$ (E_R = 40 meV and α_R = 1.6 eV·Å),[35] 2D (4-aminotetrahydropyran)$_2$PbBr$_4$ (E_R = 41 meV and α_R = 0.65 eV·Å)[75] and 3D (methylphoshonium)SnBr$_3$ (E_R = 3.3 meV and α_R = 0.62 eV Å).[76] It is evident that reducing the dimensionality from 3D and 2D to 1D can improve the air stability substantially, maintaining at the same time the beneficent spin splitting features.

The calculated charge-carrier effective masses around the valence band maximum (VBM) and the conduction band minimum (CBM) of (R-/S-THBTD)SbBr$_5$ are found to be approximately 2.15/2.75 m$_0$ and 3.5/7.16 m$_0$ for electrons and holes, respectively. The total and projected density of states are plotted in Figure S7. For both materials, the conduction band region near the CBM is dominated by the $5p$ orbitals of the Sb atoms and the $4p$ orbitals of Br atoms, similar to other metal halide semiconductors. On the other hand, the region near the VBM, the states are dominated by the $4p$ orbitals of the Br atoms, with a lesser contribution from the p orbitals of C, N, and S atoms. Unlike in other metal halide perovskites, these states belong to the species composing the organic chiral linker and are close to the VBM edge, which suggests that they might contribute to some extent to the electrical and optical properties of the materials.

We have also calculated the dielectric function and the optical absorption coefficients as a function of the incident photon energy, within the independent particle approximation, as shown in Figure S8. The static dielectric constants of both materials (Figure S8a) are almost identical with values of 4.22 and 3.98 for (R-THBTD)SbBr$_5$ and (S-THBTD)SbBr$_5$, respectively. The real and imaginary parts of dielectric function of (R-THBTD)SbBr$_5$ are slightly red-shifted compared to those of (S-THBTD)SbBr$_5$, consistent with the difference in the band gaps of the two materials. As the photon energy increases, $Re(\varepsilon)$ of both compounds exhibits

prominent sharp peak around 2.4 eV, reaching its maximum value, and two additional peaks in the range of 3.8-4.4 eV, and 7-7.8 eV and then decreases. The imaginary part and the absorption coefficient show two main peaks in the range of 2-5 eV for both materials (Figure S8). The peaks at maximum values of 2.7 and 2.9 eV indicate electronic transitions from the occupied Br($4p$) energy states of the valence band to unoccupied $4p$ and $5p$ states of Br and Sb atoms, respectively. The peaks at around 4.3 and 4.5 eV correspond to the transitions from the occupied Br($4p$) states in the valence bands to the unoccupied C(p) states in the conduction region. The results indicate that the compounds may be appropriate for visible-light and UV optoelectronic applications.

Optical absorption and photoluminescence

UV-VIS diffuse reflection spectra of (R-/S-THBTD)SbBr$_5$ reveal a sharp absorption edge for both analogs (Figure 7a), while Tauc plots validate the presence of both a direct and indirect bandgap, corroborating the DFT studies (Figure S9). Apparently, for the indirect transition (Figures S9a, b) corresponding bandgap values are 2.65 eV and 2.62 eV for the S and R analogs, while for the direct transition determined values are 2.82 eV and 2.80 eV for the S and R analogs respectively (Figures S9b, c). Evidently, the S enantiomer features a slightly higher bandgap than the R enantiomer, a trend that is further supported by the DFT studies (see above). This indicates the presence of a potential miniscule distortion of the inorganic part of the S analog over the R one. However, this is not evident by just comparing the corresponding Δd and σ^2 values for the two analogs, which are exactly the same. In halide perovskites, it has been demonstrated that the higher the octahedral distortion the wider the band gap, due to the reduction of the orbital overlap among the metal's s orbitals and halogen's p orbitals.[77-78]

Upon excitation of the as made crystals at 360 nm (R-/S-THBTD)SbBr$_5$ exhibit broad, band edge light emission centered at 460 nm (2.69 eV) and 466nm (2.66 eV) for the S and R analog respectively (Figure 7a). The observed values are consistent with recorded bandgap energies, suggesting a band edge light emission mechanism. Corresponding emission peaks exhibit a full width at half maximum (FWHM) of 71 nm for the S and 70 nm for the R analog. We ascribe the broad character of the PL

peaks to the nature of the bandgap which features both direct and indirect transitions within a close energy range.

Multiexponential fitting of the PL decay curves from time resolved PL (TRPL) studies revealed two decay constants of 0.4 ns and 3.9 ns for *R* enantiomer, while for the *S* material similar values were recorded at 0.5 ns and 3.9 ns (Figure S10). Photoluminescence excitation (PLE) studies support a uniform emission peak profile centered at 460 nm and 465 nm for *S* and *R*, upon exciting the samples from 350 nm to 385 nm (Figure 7b), which is the same for both compounds. Interestingly, metal halides that display this type of 1D corrugated structural motif usually exhibit broad white light emission, such as [(H$_2$O)-(C$_6$H$_8$N$_3$)$_2$Pb$_2$Br$_{10}$],[79] (3AMP)BiI$_5$, (3AMPY)BiI$_5$, (4AMP)BiI$_5$ and (3AMPY)BiI$_5$) (AMP = (aminomethyl)piperidinium, AMPY = (aminomethyl)-pyridinium).[73] In the latter cases, broad emission is ascribed to the presence of self-trapped excitons (STEs) (transient lattice defects that trap generated carriers), which relates closely to the distortion of the inorganic lattice.[80] Apparently, despite the noticeable distortion of the inorganic chain in (*R*-/*S*-THBTD)SbBr$_5$, band-edge emission seem to dominate, similarly to the case of 2D Cs$_3$Sb$_2$I$_9$, which exhibits asymmetric band edge PL emission.[81]

It is pointed out, that after 1 year air exposure, the absorption, TRPL, PL and PLE emission spectra of the *S* analog are intact demonstrating the robustness of the optical properties (Figures 7c,d and S11). Notably, the recorded stability performance is among the best reported for lead-free metal halide semiconductors.[61, 63, 82]

CD and SHG studies

Diffuse-reflectance CD (DRCD) measurements using powder samples revealed CD signals symmetrical to each other (mirrored), as expected for enantiomers. In particular, (*R*-/*S*-THBTD)SbBr$_5$ exhibit multiple CD peaks located at 406 nm, 326 nm, 253nm and 218nm. A zero crossing of the CD spectra in the vicinity of the corresponding absorption edge at 448nm (Figures 7a, 8a) was observed, along with the inversion of their positive or negative signals, which is known as the Cotton effect.[83] Completely different CD spectra for the hybrid semiconductors versus the chiral molecules *S*-THBTD and *R*-THBTD indicate that the CD signals do not derive by states of the chiral organic cations, but rather by perturbation of the energy states constituting the band edges of the chiral material (Figure S12).[48] Anisotropy factors

(g_{CD}) were calculated from the wavelength range of 500−200 nm. The maximum anisotropy factor of (*S*-THBTD)SbBr$_5$ and (*R*-THBTD)SbBr$_5$ was 3.4×10^{-4} and 4.9×10^{-4} at 324 nm, respectively, comparable in magnitude to values observed in other low dimensional metal halide semiconductors.[50, 84]

Second Harmonic Generation (SHG) is a nonlinear optical process in which a photon with frequency ω interacts with matter and generates a photon with doubled frequency (2ω). In the electric dipole approximation, only materials with broken inversion symmetry possess the 2nd-order nonlinearity.[85] To measure the angle resolved SHG we used a femtosecond oscillator laser that delivered pulses of 120 fs at 800 nm and at a 80 MHz repetition rate. The excitation beam polarization was controlled by a halfwave plate and in the detection (SHG) part a polarizer was used in the co-polarization configuration (Figure S13a). The laser beam was focused onto the sample by a 20x-objective. Both *R* and *S* show efficient SHG with the expected quadratic dependence of the emitted 400 nm SH light on the applied laser power (Figure S13b). The rotational anisotropy of the SH intensity was measured by the azimuthal angle φ for selected input and output polarizations. As shown in Figures 8b and c, the strongest SH response is observed for parallel polarization configuration at 45° and 90° azimuth angles for the (*S*-THBTD)SbBr$_5$ and (*R*-THBTD)SbBr$_5$ enantiomers, respectively. See Supporting Information for additional data and more details on the optical setup. While the SHG signal of the *S*- sample shows a strong anisotropic with 4-lobs SHG in the polar plot, the SHG signal of the *R*- sample only shows 2-lobs SHG indicating the breaking of inversion symmetry in the *b*-axis only.

PFM studies

The piezoelectricity of (*R*-/*S*-THBTD)SbBr$_5$ as the result of the non-centrosymmetric crystal structure of the chiral material was further confirmed by PFM measurements on corresponding thin film samples following the method we demonstrated before.[68] Stiff conductive AFM cantilevers (spring constant ~ 3 N/m) were used to minimize the electrostatic contribution to the overall signal and thus to eliminate potential artifacts in the PFM data.[86-89] We further harness the AFM cantilever resonance to enhance the electromechanical piezoresponse signal[90] and to suppress the electrostatic component via dynamic stiffening.[86] At randomly selected points on each sample, the PFM amplitude *A* was recorded as a function of the

driving frequency ω in a frequency range that contains the first contact resonance ω_0 of the AFM cantilever. The AFM cantilever dynamics can be modeled by a damped simple harmonic oscillator (DSHO)[68, 90-91]

$$A(\omega) = \frac{A_{piezo}\,\omega_0^2}{\sqrt{\left(\omega^2 - \omega_0^2\right)^2 + \left(\omega\,\omega_0/Q\right)^2}},$$

where Q and A_{piezo} are the quality factor of the resonance peak and the piezoresponse signal, respectively. Figures 9a and b show representative PFM spectra from R- and S- samples, respectively. Both spectra manifest symmetric resonance peak well-fitted by the DSHO model with no frequency-dependent background when ω is away from the cantilever resonance. Furthermore, the extracted A_{piezo} are linearly correlated to the applied alternating current (AC) bias for both R- and S- samples (Figures 9c and d). Other mechanisms that can give an PFM signal have either a non-symmetric resonance peak with frequency-dependent background (ion-migration induced Vegard strain) or a nonlinear A_{piezo} vs. V_{AC} relationship (electrostriction or induced polarization).[86, 91-93] These results suggest that the PFM measured piezoresponse signal indeed arises from the piezoelectricity of (R-/S-THBTD)SbBr$_5$ due to the polar crystal structure.[68] The confirmed piezoelectricity in our materials can further extend their application into areas where electromechanical coupling of semiconductor materials is crucial, e.g., motion energy harvesting.[94]

CONCLUSIONS

Two new 1D chiral MHS, namely (R-/S-THBTD)SbBr$_5$, were synthesized using an unexplored organic counter cation (THBTD) as structure directing agent. We elucidate the optical and electronic properties of the two enantiomers, where they both feature direct and indirect bandgap character, exhibiting broad, band edge light emission at RT that is accompanied by a lifetime of 4 ns. CD, SHG and PFM studies validate their chiral nature, while DFT calculations uncovered the corresponding R/D energy spin split performance. The corresponding E_R and α_R values are similar to those of 3D and 2D perovskite materials, demonstrating that low dimensional, lead-free MHS pose as excellent candidates for spintronic applications. Their potential is further supported by the unparallel one year air stability of (S-THBTD)SbBr$_5$, a record trait among chiral, lead-free MHS.

ASSOCIATED CONTENT

Supporting Information

Materials and methods, synthetic details, additional supplementary figures and tables about material characterization, X-ray diffraction measurements, photoluminescence measurements, thermogravimetric analysis, EDS, SEM studies, TRPL, and DFT studies.

Accession Codes

CCDC 2287819-21 contain the supplementary crystallographic data for this paper. These data can be obtained free of charge via www.ccdc.cam.ac.uk/data_request/cif,orbyemailingdata_request@ccdc.cam.ac.uk, or by contacting The Cambridge Crystallographic Data Centre, 12 Union Road, Cambridge CB2 1EZ, UK; fax: +44 1223 336033.

AUTHOR INFORMATION

Corresponding Authors

spanopoulos@usf.edu

n.zibouche@lancaster.ac.uk

Notes

The authors declare no competing financial interest.

REFERENCES

1.   Koji, Y.; Hiroshi, K.; Takashi, M.; Tsutomu, O.; Sumio, I., Structural Phase Transition and Electrical Conductivity of the Perovskite $CH_3NH_3Sn_{1-x}Pb_xBr_3$ and $CsSnBr_3$. *Bull. Chem. Soc. Jpn.* **1990,** *63* (9), 2521-2525.

2.   Stoumpos, C. C.; Malliakas, C. D.; Kanatzidis, M. G., Semiconducting Tin and Lead Iodide Perovskites with Organic Cations: Phase Transitions, High Mobilities, and Near-Infrared Photoluminescent Properties. *Inorg. Chem.* **2013,** *52* (15), 9019-9038.

3.   Jeon, N. J.; Noh, J. H.; Yang, W. S.; Kim, Y. C.; Ryu, S.; Seo, J.; Seok, S. I., Compositional Engineering of Perovskite Materials for High-performance Solar Cells. *Nature* **2015,** *517*, 476.

4.   Tsai, H.; Nie, W.; Blancon, J.-C.; Stoumpos, C. C.; Asadpour, R.; Harutyunyan, B.; Neukirch, A. J.; Verduzco, R.; Crochet, J. J.; Tretiak, S.; Pedesseau, L.; Even, J.; Alam, M. A.; Gupta, G.; Lou, J.; Ajayan, P. M.; Bedzyk, M. J.; Kanatzidis, M. G.; Mohite, A. D., High-efficiency Two-dimensional Ruddlesden–Popper Perovskite Solar Cells. *Nature* **2016,** *536*, 312.

5.   Ren, K.; Yue, S.; Li, C.; Fang, Z.; Gasem, K. A. M.; Leszczynski, J.; Qu, S.; Wang, Z.; Fan, M., Metal halide perovskites for photocatalysis applications. *J. Mater. Chem. A* **2022,** *10* (2), 407-429.

6.   Hong, Z.; Chong, W. K.; Ng, A. Y. R.; Li, M.; Ganguly, R.; Sum, T. C.; Soo, H. S., Hydrophobic Metal Halide Perovskites for Visible-Light Photoredox C−C Bond Cleavage and Dehydrogenation Catalysis. *Angew. Chem. Int. Ed.* **2019,** *58* (11), 3456-3460.

7.   He, Y.; Ke, W.; Alexander, G. C. B.; McCall, K. M.; Chica, D. G.; Liu, Z.; Hadar, I.; Stoumpos, C. C.; Wessels, B. W.; Kanatzidis, M. G., Resolving the Energy of γ-Ray Photons with $MAPbI_3$ Single Crystals. *ACS Photonics* **2018,** *5* (10), 4132-4138.

8.   He, X.; Deng, Y.; Ouyang, D.; Zhang, N.; Wang, J.; Murthy, A. A.; Spanopoulos, I.; Islam, S. M.; Tu, Q.; Xing, G.; Li, Y.; Dravid, V. P.; Zhai, T., Recent Development of Halide Perovskite Materials and Devices for Ionizing Radiation Detection. *Chem. Rev.* **2023,** *123* (4), 1207-1261.

9.   Liu, X.-K.; Xu, W.; Bai, S.; Jin, Y.; Wang, J.; Friend, R. H.; Gao, F., Metal halide perovskites for light-emitting diodes. *Nat. Mater.* **2021,** *20* (1), 10-21.

10.   Zhu, H.; Fu, Y.; Meng, F.; Wu, X.; Gong, Z.; Ding, Q.; Gustafsson, M. V.; Trinh, M. T.; Jin, S.; Zhu, X. Y., Lead halide perovskite nanowire lasers with low lasing thresholds and high quality factors. *Nat. Mater.* **2015,** *14* (6), 636-642.

11.   Katan, C.; Mercier, N.; Even, J., Quantum and Dielectric Confinement Effects in Lower-Dimensional Hybrid Perovskite Semiconductors. *Chem. Rev.* **2019,** *119* (5), 3140-3192.

12.   Mao, L.; Stoumpos, C. C.; Kanatzidis, M. G., Two-Dimensional Hybrid Halide Perovskites: Principles and Promises. *J. Am. Chem. Soc.* **2019,** *141* (3), 1171-1190.

13.   Tu, Q.; Spanopoulos, I.; Hao, S.; Wolverton, C.; Kanatzidis, M. G.; Shekhawat, G. S.; Dravid, V. P., Out-of-Plane Mechanical Properties of 2D Hybrid Organic–Inorganic Perovskites by Nanoindentation. *ACS Appl. Mater. Interfaces* **2018,** *10* (26), 22167-22173.

14.   Tu, Q.; Spanopoulos, I.; Yasaei, P.; Stoumpos, C. C.; Kanatzidis, M. G.; Shekhawat, G. S.; Dravid, V. P., Stretching and Breaking of Ultrathin 2D Hybrid Organic–Inorganic Perovskites. *ACS Nano* **2018,** *12* (10), 10347-10354.

15.   Leng, K.; Abdelwahab, I.; Verzhbitskiy, I.; Telychko, M.; Chu, L.; Fu, W.; Chi, X.; Guo, N.; Chen, Z.; Chen, Z.; Zhang, C.; Xu, Q.-H.; Lu, J.; Chhowalla, M.; Eda, G.; Loh, K. P., Molecularly Thin two-dimensional Hybrid Perovskites with Tunable Optoelectronic Properties due to Reversible Surface Relaxation. *Nat. Mater.* **2018,** *17* (10), 908-914.

16.   Chouhan, L.; Ghimire, S.; Subrahmanyam, C.; Miyasaka, T.; Biju, V., Synthesis, Optoelectronic Properties and Applications of Halide Perovskites. *Chem. Soc. Rev.* **2020,** *49* (10), 2869-2885.

17.   Manser, J. S.; Christians, J. A.; Kamat, P. V., Intriguing Optoelectronic Properties of Metal Halide Perovskites. *Chem. Rev.* **2016,** *116* (21), 12956-13008.

18.   Li, D.; Liu, X.; Wu, W.; Peng, Y.; Zhao, S.; Li, L.; Hong, M.; Luo, J., Chiral Lead-Free Hybrid Perovskites for Self-Powered Circularly Polarized Light Detection. *Angew. Chem. Int. Ed.* **2021,** *60* (15), 8415-8418.

19.   Chen, C.; Gao, L.; Gao, W.; Ge, C.; Du, X.; Li, Z.; Yang, Y.; Niu, G.; Tang, J., Circularly polarized light detection using chiral hybrid perovskite. *Nat. Commun.* **2019,** *10* (1), 1927.

20.   Xu, J.; Li, X.; Xiong, J.; Yuan, C.; Semin, S.; Rasing, T.; Bu, X.-H., Halide Perovskites for Nonlinear Optics. *Adv. Mater.* **2020,** *32* (3), 1806736.

21.   Xin, M.; Cheng, P.; Han, X.; Shi, R.; Zheng, Y.; Guan, J.; Chen, H.; Wang, C.; Liu, Y.; Xu, J.; Bu, X.-H., Resonant Second Harmonic Generation in Proline Hybrid Lead Halide Perovskites. *Adv. Opt. Mater.* **2023,** *11* (8), 2202700.

22.   Park, H.; Ha, C.; Lee, J.-H., Advances in piezoelectric halide perovskites for energy harvesting applications. *J. Mater. Chem. A* **2020,** *8* (46), 24353-24367.

23.   Qin, Y.; Gao, F.-F.; Qian, S.; Guo, T.-M.; Gong, Y.-J.; Li, Z.-G.; Su, G.-D.; Gao, Y.; Li, W.; Jiang, C.; Lu, P.; Bu, X.-H., Multifunctional Chiral 2D Lead Halide Perovskites with Circularly Polarized Photoluminescence and Piezoelectric Energy Harvesting Properties. *ACS Nano* **2022,** *16* (2), 3221-3230.

24.   Wei, Q.; Ning, Z., Chiral Perovskite Spin-Optoelectronics and Spintronics: Toward Judicious Design and Application. *ACS Mater. Lett.* **2021,** *3* (9), 1266-1275.

25.   Long, G.; Jiang, C.; Sabatini, R.; Yang, Z.; Wei, M.; Quan, L. N.; Liang, Q.; Rasmita, A.; Askerka, M.; Walters, G.; Gong, X.; Xing, J.; Wen, X.; Quintero-Bermudez, R.; Yuan, H.; Xing, G.; Wang, X. R.; Song, D.; Voznyy, O.; Zhang, M.; Hoogland, S.; Gao, W.; Xiong, Q.; Sargent, E. H., Spin control in reduced-dimensional chiral perovskites. *Nat. Photonics* **2018,** *12* (9), 528-533.

26.   Wang, J.; Zhang, C.; Liu, H.; Liu, X.; Guo, H.; Sun, D.; Vardeny, Z. V., Tunable Spin Characteristic Properties in Spin Valve Devices Based on Hybrid Organic–Inorganic Perovskites. *Adv. Mater.* **2019,** *31* (41), 1904059.

27.   Wang, J.; Lu, H.; Pan, X.; Xu, J.; Liu, H.; Liu, X.; Khanal, D. R.; Toney, M. F.; Beard, M. C.; Vardeny, Z. V., Spin-Dependent Photovoltaic and Photogalvanic Responses of Optoelectronic Devices Based on Chiral Two-Dimensional Hybrid Organic–Inorganic Perovskites. *ACS Nano* **2021,** *15* (1), 588-595.

28.   Lu, H.; Wang, J.; Xiao, C.; Pan, X.; Chen, X.; Brunecky, R.; Berry, J. J.; Zhu, K.; Beard, M. C.; Vardeny, Z. V., Spin-dependent charge transport through 2D chiral hybrid lead-iodide perovskites. *Sci. Adv.* **2019,** *5* (12), eaay0571.

29.   Wang, F.; Gao, H.; de Graaf, C.; Poblet, J. M.; Campbell, B. J.; Stroppa, A., Switchable Rashba anisotropy in layered hybrid organic–inorganic perovskite by hybrid improper ferroelectricity. *Npj Comput. Mater.* **2020,** *6* (1), 183.

30.   Jana, M. K.; Song, R.; Liu, H.; Khanal, D. R.; Janke, S. M.; Zhao, R.; Liu, C.; Valy Vardeny, Z.; Blum, V.; Mitzi, D. B., Organic-to-inorganic structural chirality transfer in a 2D hybrid perovskite and impact on Rashba-Dresselhaus spin-orbit coupling. *Nat. Commun.* **2020,** *11* (1), 4699.

31.   Jana, M. K.; Song, R.; Xie, Y.; Zhao, R.; Sercel, P. C.; Blum, V.; Mitzi, D. B., Structural descriptor for enhanced spin-splitting in 2D hybrid perovskites. *Nat. Commun.* **2021,** *12* (1), 4982.

32.   Odenthal, P.; Talmadge, W.; Gundlach, N.; Wang, R.; Zhang, C.; Sun, D.; Yu, Z.-G.; Valy Vardeny, Z.; Li, Y. S., Spin-polarized exciton quantum beating in hybrid organic–inorganic perovskites. *Nature Physics* **2017,** *13* (9), 894-899.

33.   Kim, Y.-H.; Zhai, Y.; Lu, H.; Pan, X.; Xiao, C.; Gaulding, E. A.; Harvey, S. P.; Berry, J. J.; Vardeny, Z. V.; Luther, J. M.; Beard, M. C., Chiral-induced spin selectivity enables a room-temperature spin light-emitting diode. *Science* **2021,** *371* (6534), 1129-1133.

34.   Lu, H.; Vardeny, Z. V.; Beard, M. C., Control of light, spin and charge with chiral metal halide semiconductors. *Nat. Rev. Chem.* **2022,** *6* (7), 470-485.

35.   Zhai, Y.; Baniya, S.; Zhang, C.; Li, J.; Haney, P.; Sheng, C.-X.; Ehrenfreund, E.; Vardeny, Z. V., Giant Rashba splitting in 2D organic-inorganic halide perovskites measured by transient spectroscopies. *Sci. Adv.* **2017,** *3* (7), e1700704.

36.   Xie, Y.; Song, R.; Singh, A.; Jana, M. K.; Blum, V.; Mitzi, D. B., Kinetically Controlled Structural Transitions in Layered Halide-Based Perovskites: An Approach to Modulate Spin Splitting. *J. Am. Chem. Soc.* **2022,** *144* (33), 15223-15235.

37.   Zheng, Y.; Han, X.; Cheng, P.; Jia, X.; Xu, J.; Bu, X.-H., Induction of Chiral Hybrid Metal Halides from Achiral Building Blocks. *J. Am. Chem. Soc.* **2022,** *144* (36), 16471-16479.

38.   Billing, D. G.; Lemmerer, A., Bis[(S)-[beta]-phenethylammonium] tribromoplumbate(II). *Acta Crystallogr. Sect. E* **2003,** *59* (6), m381-m383.

39.   Chen, C.; Gao, L.; Gao, W.; Ge, C.; Du, X.; Li, Z.; Yang, Y.; Niu, G.; Tang, J., Circularly polarized light detection using chiral hybrid perovskite. *Nature Communications* **2019,** *10* (1), 1927.

40.   Wang, L.; Xue, Y.; Cui, M.; Huang, Y.; Xu, H.; Qin, C.; Yang, J.; Dai, H.; Yuan, M., A Chiral Reduced-Dimension Perovskite for an Efficient Flexible Circularly Polarized Light Photodetector.

Angew. Chem. Int. Ed. **2020,** *59* (16), 6442-6450.

41.   Hao, J.; Lu, H.; Mao, L.; Chen, X.; Beard, M. C.; Blackburn, J. L., Direct Detection of Circularly Polarized Light Using Chiral Copper Chloride–Carbon Nanotube Heterostructures. *ACS Nano* **2021,** *15* (4), 7608-7617.

42.   Lu, H.; Xiao, C.; Song, R.; Li, T.; Maughan, A. E.; Levin, A.; Brunecky, R.; Berry, J. J.; Mitzi, D. B.; Blum, V.; Beard, M. C., Highly Distorted Chiral Two-Dimensional Tin Iodide Perovskites for Spin Polarized Charge Transport. *J. Am. Chem. Soc.* **2020,** *142* (30), 13030-13040.

43.   Ma, J.; Fang, C.; Chen, C.; Jin, L.; Wang, J.; Wang, S.; Tang, J.; Li, D., Chiral 2D Perovskites with a High Degree of Circularly Polarized Photoluminescence. *ACS Nano* **2019,** *13* (3), 3659-3665.

44.   Liu, T.; Shi, W.; Tang, W.; Liu, Z.; Schroeder, B. C.; Fenwick, O.; Fuchter, M. J., High Responsivity Circular Polarized Light Detectors based on Quasi Two-Dimensional Chiral Perovskite Films. *ACS Nano* **2022,** *16* (2), 2682-2689.

45.   Ahn, J.; Ma, S.; Kim, J.-Y.; Kyhm, J.; Yang, W.; Lim, J. A.; Kotov, N. A.; Moon, J., Chiral 2D Organic Inorganic Hybrid Perovskite with Circular Dichroism Tunable Over Wide Wavelength Range. *J. Am. Chem. Soc.* **2020,** *142* (9), 4206-4212.

46.   Peng, Y.; Liu, X.; Li, L.; Yao, Y.; Ye, H.; Shang, X.; Chen, X.; Luo, J., Realization of vis–NIR Dual-Modal Circularly Polarized Light Detection in Chiral Perovskite Bulk Crystals. *J. Am. Chem. Soc.* **2021,** *143* (35), 14077-14082.

47.   Li, Z.; Yan, Y.; Song, M.-S.; Xin, J.-Y.; Wang, H.-Y.; Wang, H.; Wang, Y., Exciton–Phonon Coupling of Chiral One-Dimensional Lead-Free Hybrid Metal Halides at Room Temperature. *J. Phys. Chem. Lett.* **2022,** *13* (18), 4073-4081.

48.   Liu, S.; Heindl, M. W.; Fehn, N.; Caicedo-Dávila, S.; Eyre, L.; Kronawitter, S. M.; Zerhoch, J.; Bodnar, S.; Shcherbakov, A.; Stadlbauer, A.; Kieslich, G.; Sharp, I. D.; Egger, D. A.; Kartouzian, A.; Deschler, F., Optically Induced Long-Lived Chirality Memory in the Color-Tunable Chiral Lead-Free Semiconductor (R)/(S)-CHEA4Bi2BrxI10−x (x = 0–10). *J. Am. Chem. Soc.* **2022,** *144* (31), 14079-14089.

49.   Yao, L.; Zeng, Z.; Cai, C.; Xu, P.; Gu, H.; Gao, L.; Han, J.; Zhang, X.; Wang, X.; Wang, X.; Pan, A.; Wang, J.; Liang, W.; Liu, S.; Chen, C.; Tang, J., Strong Second- and Third-Harmonic Generation in 1D Chiral Hybrid Bismuth Halides. *J. Am. Chem. Soc.* **2021,** *143* (39), 16095-16104.

50.   Moon, T. H.; Oh, S.-J.; Ok, K. M., [((R)-C8H12N)4][Bi2Br10] and [((S)-C8H12N)4][Bi2Br10]: Chiral Hybrid Bismuth Bromides Templated by Chiral Organic Cations. *ACS Omega* **2018,** *3* (12), 17895-17903.

51.   Li, J.; Guo, Z.; Li, P.; Liu, J.; Zhai, X.; Chang, Z.; Chang, W.; Long, G.; Niu, B.; Guo, Y., Magnetic Fano resonance enhanced second-harmonic generation in chiral hybrid bismuth halides. *Appl. Phys. Lett.* **2023,** *122* (9), 091701.

52.   Rajput, P. K.; Poonia, A. K.; Mukherjee, S.; Sheikh, T.; Shrivastava, M.; Adarsh, K. V.; Nag, A., Chiral Methylbenzylammonium Bismuth Iodide with Zero-Dimensional Perovskite Derivative Structure. *J. Phys. Chem. C* **2022,** *126* (23), 9889-9897.

53.   Dehnhardt, N.; Axt, M.; Zimmermann, J.; Yang, M.; Mette, G.; Heine, J., Band Gap-Tunable, Chiral Hybrid Metal Halides Displaying Second-Harmonic Generation. *Chem. Mater.* **2020,** *32* (11), 4801-4807.

54.   Yao, L.; Xue, K.-H.; Tong, H.; Chen, C.; Niu, G.; Yang, W.; Tang, J., Dimensional Control of Chiral Antimony Halide Compounds for Enhanced Circular Dichroism. *Cryst. Growth Des.* **2022,** *22* (9), 5552-5558.

55.   Wang, Z.; Zhang, Z.; Sung, H. H. Y.; Williams, I. D.; Lu, H., Structural Asymmetry and Chiroptical Activity of Chiral Antimony-Halide Hybrids. *Eur. J. Inorg. Chem.* **2022,** *2022* (23), e202200275.

56.   Qi, S.; Cheng, P.; Han, X.; Ge, F.; Shi, R.; Xu, L.; Li, G.; Xu, J., Organic–Inorganic Hybrid Antimony(III) Halides for Second Harmonic Generation. *Cryst. Growth Des.* **2022,** *22* (11), 6545-6553.

57.   Xuan, H.-L.; Li, J.-L.; Xu, L.-J.; Zheng, D.-S.; Chen, Z.-N., Circularly Polarized Luminescence based on 0D Lead-Free Antimony (III) Halide Hybrids. *Adv. Opt. Mater.* **2022,** *10* (16), 2200591.

58.   Wu, F.; Wei, Q.; Li, X.; Liu, Y.; Huang, W.; Chen, Q.; Li, B.; Luo, J.; Liu, X., Cooperative Enhancement of Second Harmonic Generation in an Organic–Inorganic Hybrid Antimony Halide. *Cryst. Growth Des.* **2022,** *22* (6), 3875-3881.

59.   Park, N.-G.; Grätzel, M.; Miyasaka, T.; Zhu, K.; Emery, K., Towards Stable and Commercially Available Perovskite Solar Cells. *Nat. Energy* **2016,** *1*, 16152.

60.   Liu, H.; Shonde, T. B.; Gonzalez, F.; Olasupo, O. J.; Lee, S.; Luong, D.; Lin, X.; Vellore Winfred, J. S. R.; Lochner, E.; Fatima, I.; Hanson, K.; Ma, B., Efficient Red Light Emitting Diodes Based on a Zero-

Dimensional Organic Antimony Halide Hybrid. *Adv. Mater.* **2023,** *35* (9), 2209417.

61.	Zhao, J.-Q.; Han, M.-F.; Zhao, X.-J.; Ma, Y.-Y.; Jing, C.-Q.; Pan, H.-M.; Li, D.-Y.; Yue, C.-Y.; Lei, X.-W., Structural Dimensionality Modulation toward Enhanced Photoluminescence Efficiencies of Hybrid Lead-Free Antimony Halides. *Adv. Opt. Mater.* **2021,** *9* (19), 2100556.

62.	Mo, Q.; Qian, Q.; Shi, Y.; Cai, W.; Zhao, S.; Zang, Z., High Quantum Efficiency of Stable Sb-Based Perovskite-Like Halides toward White Light Emission and Flexible X-Ray Imaging. *Adv. Opt. Mater.* **2022,** *10* (23), 2201509.

63.	Liu, F.; Zhang, T.; Mondal, D.; Teng, S.; Zhang, Y.; Huang, K.; Wang, D.; Yang, W.; Mahadevan, P.; Zhao, Y. S.; Xie, R.; Pradhan, N., Light-Emitting Metal–Organic Halide 1D and 2D Structures: Near-Unity Quantum Efficiency, Low-Loss Optical Waveguide and Highly Polarized Emission. *Angew. Chem. Int. Ed.* **2021,** *60* (24), 13548-13553.

64.	Tao, K.; Zhang, B.; Li, Q.; Yan, Q., Centimeter-Sized Piezoelectric Single Crystal of Chiral Bismuth-Based Hybrid Halide with Superior Electrostrictive Coefficient. *Small* **2023,** *19* (15), 2207663.

65.	Maiti, A.; Pal, A. J., Spin-Selective Charge Transport in Lead-Free Chiral Perovskites: The Key towards High-Anisotropy in Circularly-Polarized Light Detection. *Angew. Chem. Int. Ed.* **2022,** *61* (52), e202214161.

66.	Zibouche, N.; Islam, M. S., Structure–Electronic Property Relationships of 2D Ruddlesden–Popper Tin- and Lead-based Iodide Perovskites. *ACS Appl. Mater. Interfaces* **2020,** *12* (13), 15328-15337.

67.	Alonso, J. A.; Martínez-Lope, M. J.; Casais, M. T.; Fernández-Díaz, M. T., Evolution of the Jahn−Teller Distortion of MnO6 Octahedra in RMnO3 Perovskites (R = Pr, Nd, Dy, Tb, Ho, Er, Y): A Neutron Diffraction Study. *Inorg. Chem.* **2000,** *39* (5), 917-923.

68.	Du, K.-z.; Tu, Q.; Zhang, X.; Han, Q.; Liu, J.; Zauscher, S.; Mitzi, D. B., Two-Dimensional Lead(II) Halide-Based Hybrid Perovskites Templated by Acene Alkylamines: Crystal Structures, Optical Properties, and Piezoelectricity. *Inorg. Chem.* **2017,** *56* (15), 9291-9302.

69.	Robinson, K.; Gibbs, G. V.; Ribbe, P. H., Quadratic Elongation: A Quantitative Measure of Distortion in Coordination Polyhedra. *Science* **1971,** *172* (3983), 567-570.

70.	Liu, W.-T.; Zhang, Z.-X.; Ding, K.; Fu, D.-W.; Lu, H.-F., Halogen tuning toward dielectric switch and band gap engineering in one-dimensional hybrid materials. *J. Mol. Struct.* **2022,** *1270*, 133954.

71.	Han, S.; Zhang, J.; Sun, Z.; Ji, C.; Zhang, W.; Wang, Y.; Tao, K.; Teng, B.; Luo, J., Lead-Free Hybrid Material with an Exceptional Dielectric Phase Transition Induced by a Chair-to-Boat Conformation Change of the Organic Cation. *Inorg. Chem.* **2017,** *56* (21), 13078-13085.

72.	Stoumpos, C. C.; Mao, L.; Malliakas, C. D.; Kanatzidis, M. G., Structure–Band Gap Relationships in Hexagonal Polytypes and Low-Dimensional Structures of Hybrid Tin Iodide Perovskites. *Inorg. Chem.* **2017,** *56* (1), 56-73.

73.	Li, X.; Traoré, B.; Kepenekian, M.; Li, L.; Stoumpos, C. C.; Guo, P.; Even, J.; Katan, C.; Kanatzidis, M. G., Bismuth/Silver-Based Two-Dimensional Iodide Double and One-Dimensional Bi Perovskites: Interplay between Structural and Electronic Dimensions. *Chem. Mater.* **2021,** *33* (15), 6206-6216.

74.	Deng, C.; Hao, S.; Liu, K.; Molokeev, M. S.; Wolverton, C.; Fan, L.; Zhou, G.; Chen, D.; Zhao, J.; Liu, Q., Broadband light emitting zero-dimensional antimony and bismuth-based hybrid halides with diverse structures. *J. Mater. Chem. C* **2021,** *9* (44), 15942-15948.

75.	Huang, G.; Rassel, S.; Qu, J.; Xu, S.; Wang, C.; Ban, D., Manipulation of Spin Splitting in Two-Dimensional Lead Bromide Perovskite Rashba Piezoelectrics. *ACS Appl. Electron. Mater.* **2021,** *3* (1), 285-291.

76.	Kashikar, R.; Ghosh, P. S.; Lisenkov, S.; Stroppa, A.; Ponomareva, I., Rashba effects in lead-free ferroelectric semiconductor [CH$_3$PH$_3$]SnBr$_3$. *Phys. Rev. Mater.* **2022,** *6* (10), 104603.

77.	Stoumpos, C. C.; Kanatzidis, M. G., The Renaissance of Halide Perovskites and Their Evolution as Emerging Semiconductors. *Acc. Chem. Res.* **2015,** *48* (10), 2791-2802.

78.	Prasanna, R.; Gold-Parker, A.; Leijtens, T.; Conings, B.; Babayigit, A.; Boyen, H.-G.; Toney, M. F.; McGehee, M. D., Band Gap Tuning via Lattice Contraction and Octahedral Tilting in Perovskite Materials for Photovoltaics. *J. Am. Chem. Soc.* **2017,** *139* (32), 11117-11124.

79.	Biswas, A.; Bakthavatsalam, R.; Shaikh, S. R.; Shinde, A.; Lohar, A.; Jena, S.; Gonnade, R. G.; Kundu, J., Efficient Broad-Band Emission from Contorted Purely Corner-Shared One Dimensional (1D) Organic Lead Halide Perovskite. *Chem. Mater.* **2019,** *31* (7), 2253-2257.

80.	Cortecchia, D.; Neutzner, S.; Srimath Kandada, A. R.; Mosconi, E.; Meggiolaro, D.; De Angelis, F.; Soci, C.; Petrozza, A., Broadband Emission in Two-Dimensional Hybrid Perovskites: The Role of Structural Deformation. *J. Am. Chem. Soc.* **2017,** *139* (1), 39-42.

81.   Saparov, B.; Hong, F.; Sun, J.-P.; Duan, H.-S.; Meng, W.; Cameron, S.; Hill, I. G.; Yan, Y.; Mitzi, D. B., Thin-Film Preparation and Characterization of Cs3Sb2I9: A Lead-Free Layered Perovskite Semiconductor. *Chem. Mater.* **2015,** *27* (16), 5622-5632.

82.   Morad, V.; Yakunin, S.; Benin, B. M.; Shynkarenko, Y.; Grotevent, M. J.; Shorubalko, I.; Boehme, S. C.; Kovalenko, M. V., Hybrid 0D Antimony Halides as Air-Stable Luminophores for High-Spatial-Resolution Remote Thermography. *Adv. Mater.* **2021,** *33* (9), 2007355.

83.   Berova, N.; Bari, L. D.; Pescitelli, G., Application of electronic circular dichroism in configurational and conformational analysis of organic compounds. *Chem. Soc. Rev.* **2007,** *36* (6), 914-931.

84.   Ishii, A.; Miyasaka, T., Direct detection of circular polarized light in helical 1D perovskite-based photodiode. *Sci. Adv.* **2020,** *6* (46), eabd3274.

85.   Morrow, D. J.; Hautzinger, M. P.; Lafayette, D. P., II; Scheeler, J. M.; Dang, L.; Leng, M.; Kohler, D. D.; Wheaton, A. M.; Fu, Y.; Guzei, I. A.; Tang, J.; Jin, S.; Wright, J. C., Disentangling Second Harmonic Generation from Multiphoton Photoluminescence in Halide Perovskites using Multidimensional Harmonic Generation. *J. Phys. Chem. Lett.* **2020,** *11* (16), 6551-6559.

86.   Jesse, S.; Baddorf, A. P.; Kalinin, S. V., Dynamic behaviour in piezoresponse force microscopy. *Nanotechnology* **2006,** *17* (6), 1615.

87.   Kalinin, S. V.; Bonnell, D. A., Imaging mechanism of piezoresponse force microscopy of ferroelectric surfaces. *Phys. Rev. B* **2002,** *65* (12), 125408.

88.   Soergel, E., Piezoresponse force microscopy (PFM). *J. Phys. D: Appl. Phys.* **2011,** *44* (46), 464003.

89.   Eliseev, E. A.; Morozovska, A. N.; Ievlev, A. V.; Balke, N.; Maksymovych, P.; Tselev, A.; Kalinin, S. V., Electrostrictive and electrostatic responses in contact mode voltage modulated scanning probe microscopies. *Appl. Phys. Lett.* **2014,** *104* (23).

90.   Jesse, S.; Mirman, B.; Kalinin, S. V., Resonance enhancement in piezoresponse force microscopy: Mapping electromechanical activity, contact stiffness, and Q factor. *Appl. Phys. Lett.* **2006,** *89* (2).

91.   Zelisko, M.; Hanlumyuang, Y.; Yang, S.; Liu, Y.; Lei, C.; Li, J.; Ajayan, P. M.; Sharma, P., Anomalous piezoelectricity in two-dimensional graphene nitride nanosheets. *Nat. Commun.* **2014,** *5* (1), 4284.

92.   Jesse, S.; Guo, S.; Kumar, A.; Rodriguez, B. J.; Proksch, R.; Kalinin, S. V., Resolution theory, and static and frequency-dependent cross-talk in piezoresponse force microscopy. *Nanotechnology* **2010,** *21* (40), 405703.

93.   Seol, D.; Park, S.; Varenyk, O. V.; Lee, S.; Lee, H. N.; Morozovska, A. N.; Kim, Y., Determination of ferroelectric contributions to electromechanical response by frequency dependent piezoresponse force microscopy. *Sci. Rep.* **2016,** *6* (1), 30579.

94.   Sezer, N.; Koç, M., A comprehensive review on the state-of-the-art of piezoelectric energy harvesting. *Nano Energy* **2021,** *80*, 105567.
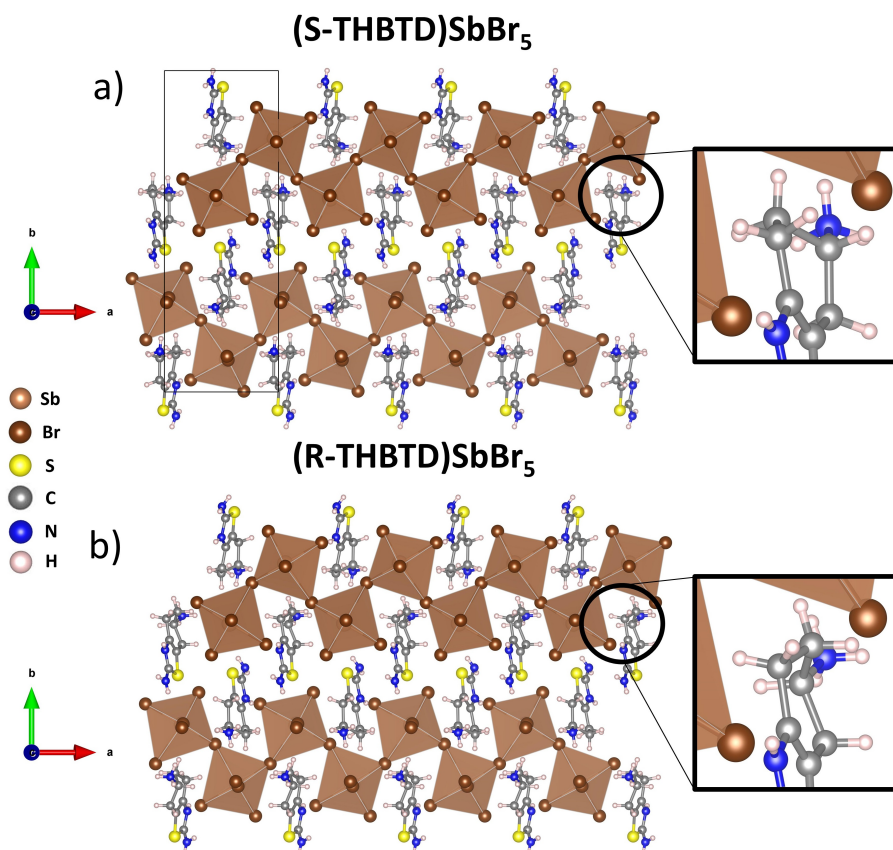
Figures

Figure 1. (a), (b) Part of the crystal structures of (*R*-/*S*-THBTD)SbBr$_5$ viewing along the *c*-axis, demonstrating the 1D corrugated inorganic chain. Inset figures highlight the difference in the configuration of the *S*-THBTD and *R*-THBTD organic molecules in the two enantiomers, (*S*-THBTD)SbBr$_5$ and (*R*-THBTD)SbBr$_5$. The unit cell in (a) is indicated by a black parallelogram.
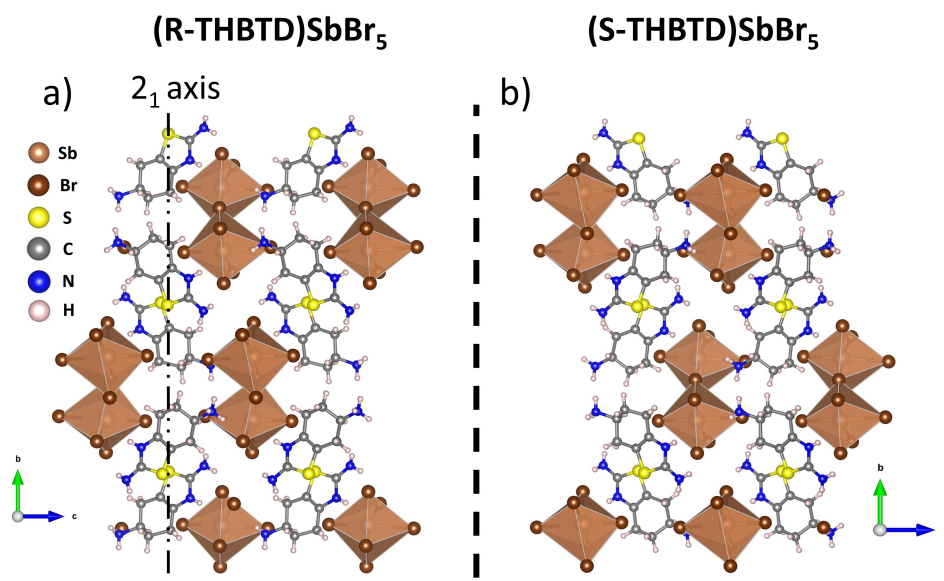
Figure 2. (a), (b) Part of the crystal structures of (*R*-/*S*-THBTD)SbBr$_5$ viewing along the α-axis, showcasing the enantiomorphic nature of the two analogs. The 2_1 screw axis that is responsible for the propagation of the organic part of the structure is highlighted with a dash and dot line.
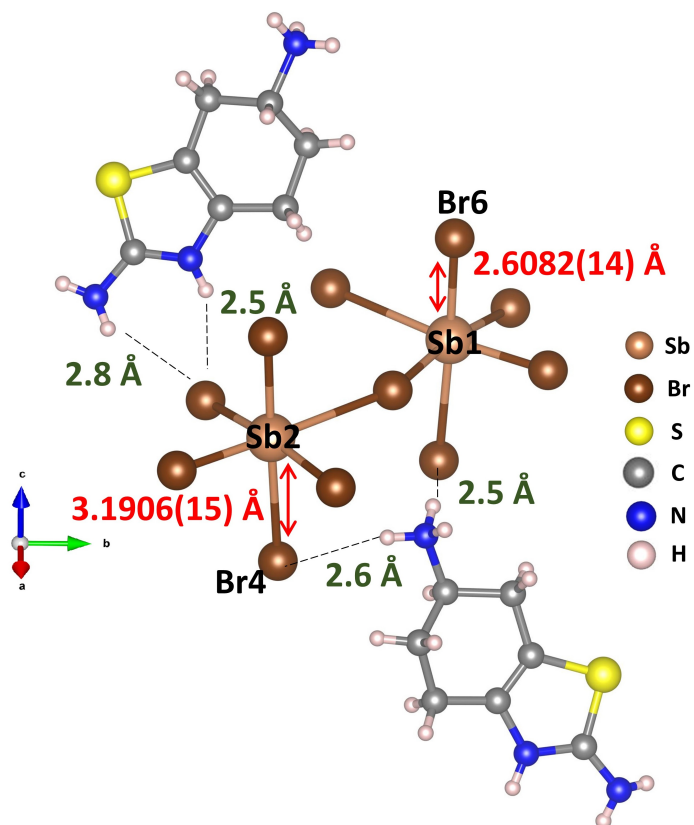
Figure 3. Representation of part of the (*R*-THBTD)SbBr$_5$ structure, demonstrating the number and magnitude of the hydrogen bonds that are responsible for the octahedra distortion. Corresponding hydrogen bond distances range from 2.5 Å to 2.8 Å, among the hydrogen atoms of the three amine functional groups (R-NH$_2$, RNH$_3$, -NH=) of the organic counter-cations and the axial and equatorial bromide atoms of the [SbBr$_6$]$^{3-}$ octahedra.
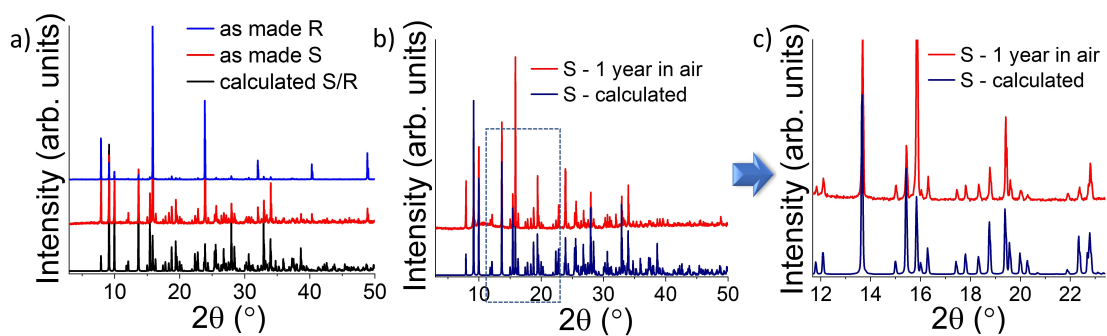
Figure 4. (a) Comparison of the PXRD patterns for the as made (*R*-/*S*-THBTD)SbBr$_5$ compounds to the calculated pattern based from the solved single crystal structure. (b) Comparison of the PXRD patterns for the (*S*-THBTD)SbBr$_5$ after 1 year air exposure (*RH* = 35-55% ± 5%) to the calculated pattern based from the solved single crystal structure. (c) Zoom into the highlighted area of the PXRD patterns from 11° to 23° 2θ verifying the high crystallinity, phase purity and structural integrity of the air treated sample.
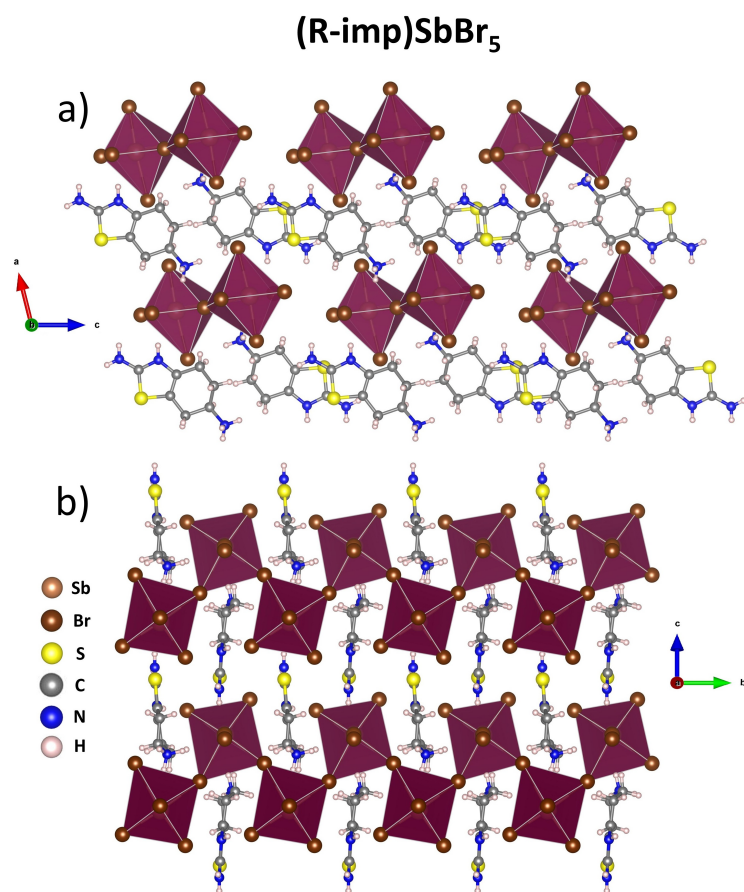
(R-imp)SbBr$_5$

Figure 5. (a) Part of the crystal structures of impurity phase (*R*-imp)SbBr$_5$ viewing along the *b*-axis and (b) *α*-axis. The structure consists of the same 1D corrugated inorganic chain of corner sharing [SbBr$_6$]$^{3-}$ octahedra as the pure enantiomers, albeit much less distorted.
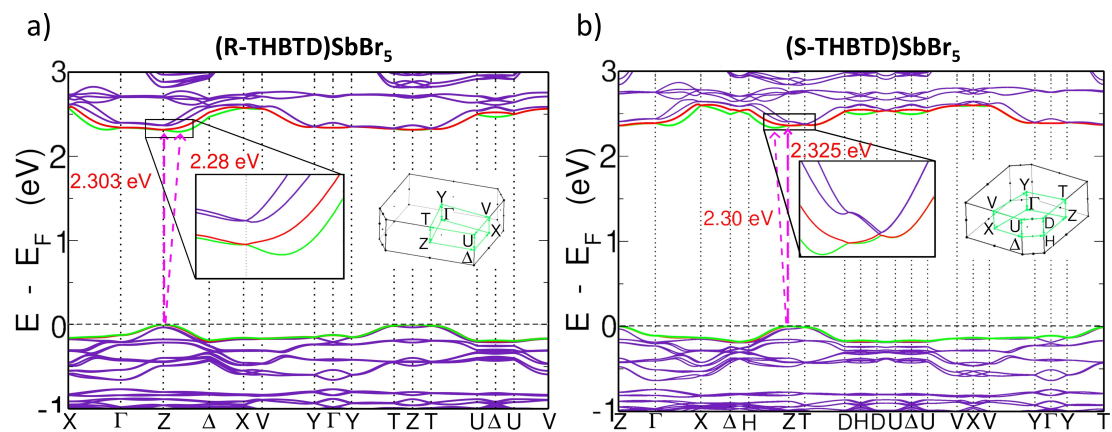
Figure 6. Band structures of (a) (R-THBTD)SbBr$_5$ and (b) (S-THBTD)SbBr$_5$ compounds depicting the band energy split due to the non-centrosymmetric nature of the materials.
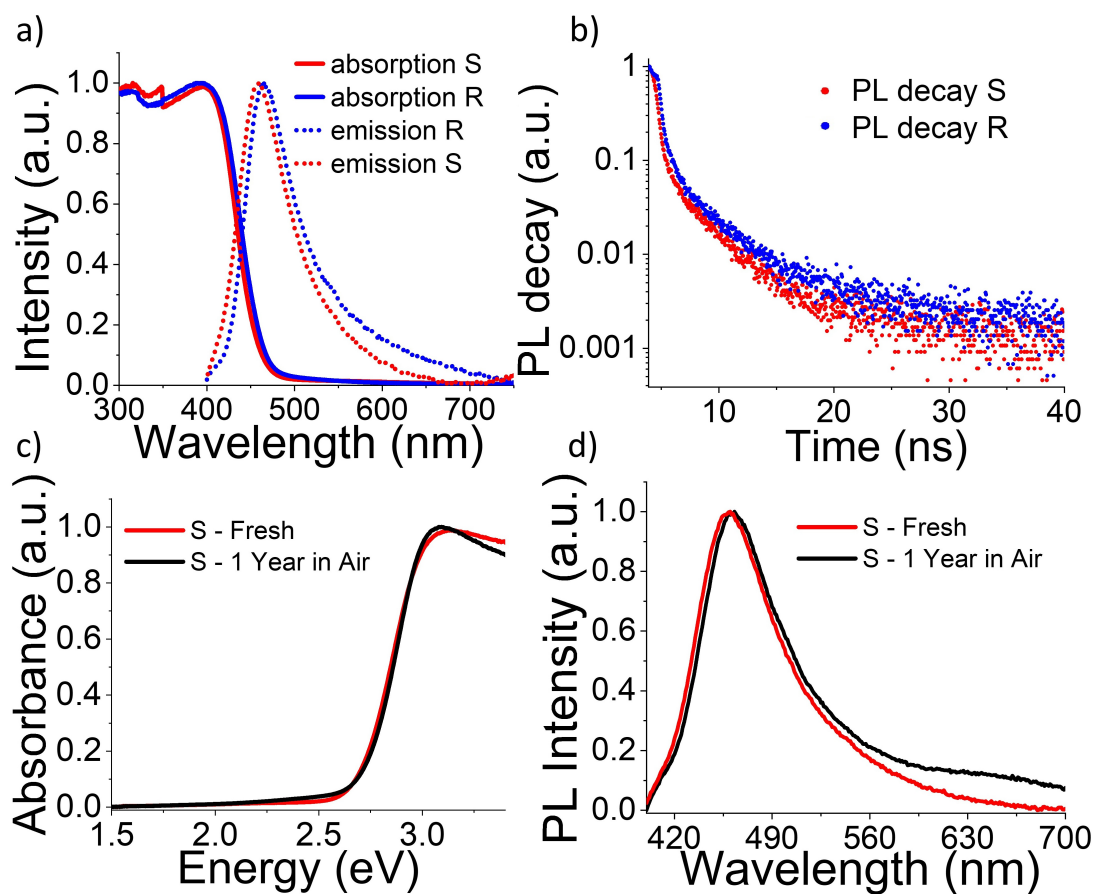
Figure 7. (a) The recorded absorption and emission spectra of (*R*-/*S*-THBTD)SbBr$_5$ compounds at RT, b) TRPL decay curves of the pristine material at RT, comparison of absorbance (c) and PL spectra (d) for the fresh sample and the air treated one. The material maintains its optical properties after 1 year exposure in air.
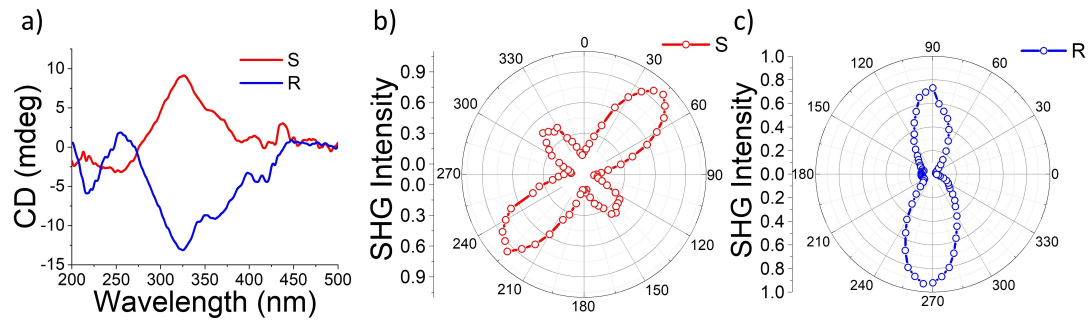
Figure 8. (a) DRCD spectra for the (*R*-THBTD)SbBr$_5$ and (*S*-THBTD)SbBr$_5$ materials. (b) Azimuth SHG signal in the parallel polarization configuration for (*S*-THBTD)SbBr$_5$ and (c) (*R*-THBTD)SbBr$_5$ as a function of polarization angle.
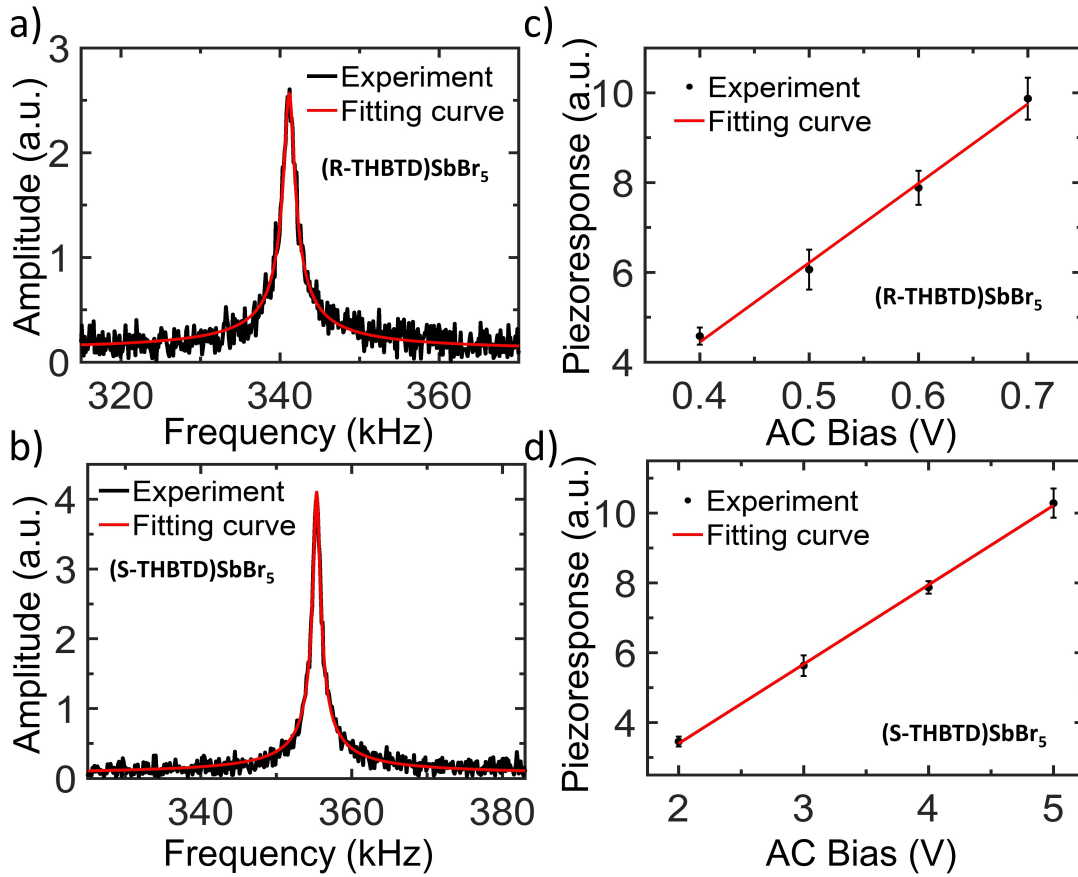
Figure 9. Representative AFM cantilever vibration amplitude *vs.* AC driving frequency spectra around the first contact resonance peak from PFM measurements of (a) (*R*-THBTD)SbBr$_5$ and (b) (*S*-THBTD)SbBr$_5$. The red curve indicates DHSO model fitting. (c) and (d) are the extracted piezoresponses from (*R*-THBTD)SbBr$_5$ and (*S*-THBTD)SbBr$_5$, respectively, plotted as a function of the AC bias voltage. The red lines indicate the linear fitting.

Table 1. Crystal and structure refinement data for (*R*-THBTD)SbBr$_5$, (*S*-THBTD)SbBr$_5$ and (*R*-imp)SbBr$_5$ at 296 K.

Compound	(*R*-THBTD)SbBr$_5$	(*S*-THBTD)SbBr$_5$	(*R*-imp)SbBr$_5$
Crystal system	monoclinic	monoclinic	monoclinic
Space group	*P*2$_1$	*P*2$_1$	*P*2$_1$
Unit cell dimensions	$a = 8.0595(11)$ Å, $\alpha = 90°$ $b = 22.371(3)$ Å, $\beta = 99.224(2)°$ $c = 9.8016(13)$ Å, $\gamma = 90°$	$a = 8.0556(5)$ Å, $\alpha = 90°$ $b = 22.3743(13)$ Å, $\beta = 99.2680(10)°$ $c = 9.7987(6)$ Å, $\gamma = 90°$	$a = 9.7928(8)$ Å, $\alpha = 90°$ $b = 7.6749(6)$ Å, $\beta = 104.1260(10)°$ $c = 11.5269(9)$ Å, $\gamma = 90°$
Volume	1744.4(4) Å^3	1743.05(18) Å^3	840.15(12) Å^3
Z	4	4	2
Density (calculated)	2.637 g/cm^3	2.639 g/cm^3	2.738 g/cm^3
Independent reflections	8637 [$R_{int} = 0.0396$]	8602 [$R_{int} = 0.0322$]	3962 [$R_{int} = 0.0391$]
Completeness to $\theta = 29.33°$	100%	100%	100%
Data / restraints / parameters	8637 / 8 / 328	8602 / 8 / 328	3962 / 5 / 178
Goodness-of-fit	0.994	1.020	0.901
Final R indices [$I>2\sigma(I)$]	$R_{obs} = 0.0374$, w$R_{obs} = 0.0620$	$R_{obs} = 0.0322$, w$R_{obs} = 0.0606$	$R_{obs} = 0.0301$, w$R_{obs} = 0.0497$
R indices [all data]	$R_{all} = 0.0644$, w$R_{all} = 0.0689$	$R_{all} = 0.0445$, w$R_{all} = 0.0644$	$R_{all} = 0.0425$, w$R_{all} = 0.0536$
Largest diff. peak and hole	0.959 and -0.937 e·Å^{-3}	1.019 and -0.924 e·Å^{-3}	0.497 and -0.565 e·Å^{-3}
Flack parameter	0.028(15)	0.023(14)	0.019(10)

$R = \Sigma||F_o|-|F_c|| / \Sigma|F_o|$, w$R = (\Sigma[w(|F_o|^2 - |F_c|^2)^2] / \Sigma[w(|F_o|^4)])^{1/2}$ and w$=1/(\sigma^2(I)+0.0004I^2)$

Table of Contents Graphic
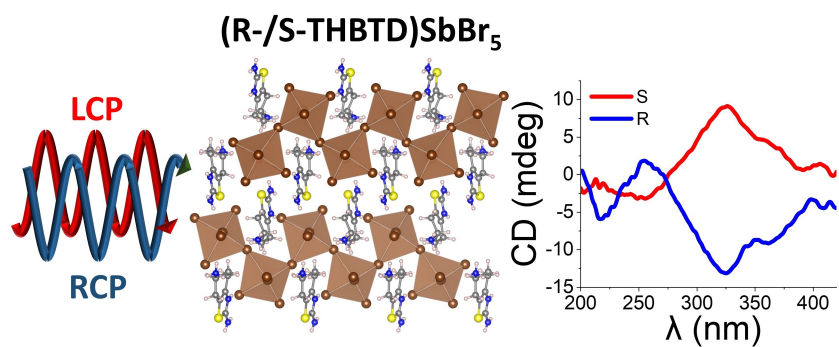
(R-/S-THBTD)SbBr$_5$

Synopsis: We report the synthesis, characterization and optical properties of two new 1D chiral MHS, namely (*R-/S*-THBTD)SbBr$_5$. The corresponding materials exhibit broad, band edge light emission at RT, and are air stable for a year. DFT calculations uncovered the corresponding R/D energy spin split performance, demonstrating that low dimensional, lead-free MHS pose as excellent candidates for spintronic applications.